

1 **Analysis of Galileo IOV+FOC Signals and E5 RTK performance**

2

3 Safoora Zaminpardaz¹ and Peter J.G. Teunissen^{1,2}

4

5 ¹GNSS Research Centre

6 Curtin University

7 GPO Box U1987

8 Perth WA 6845

9 Australia

10

11 ²Department of Geoscience and Remote Sensing

12 PO Box 5048

13 2600 GA Delft

14 The Netherlands

15

16

17 Corresponding author: S. Zaminpardaz

18 Email: safoora.zaminpardaz@postgrad.curtin.edu.au

19 Tel.: +61 8 9266 3157

20 Fax: +61 8 9266 2703

21

22

23

24 **Abstract** The current Galileo constellation in April 2017 comprises both IOV (In-Orbit
25 validation) and FOC (Full Operational Capability) satellites transmitting signals on five
26 frequencies, i.e. E1, E5a, E5b, E5, and E6. We analyze the power, multipath and noise of

27 these signals using the data collected by four short baselines of various lengths and
28 receiver/antenna types in Perth, Australia as well as the Netherlands. In our analysis, the
29 Galileo signals, except E5, show different relative noise and multipath performance for
30 different receiver/antenna types. The E5 signal, with a weak dependency on the type of
31 receiver/antenna, shows a significantly lower level of multipath and noise with respect to the
32 other signals. Estimations of the E5 code standard deviation based on the data of each of the
33 mentioned baselines gives a value of about 6 cm, which is further reduced to about 1 cm once
34 the data are corrected for multipath. Due to the superior stochastic properties of E5 signal
35 compared to the other Galileo signals, we further analyze the short-baseline RTK (Real-Time
36 Kinematic) performance of the Galileo standalone E5 observations. Our findings confirm that
37 the Galileo E5 data, if corrected for the multipath effect, can make (almost) instantaneous
38 ambiguity resolution feasible already based on the current constellation.

39

40 **Keywords** Galileo, IOV, FOC, E5AltBOC, Signal power, Multipath, Noise characteristics,
41 Integer ambiguity resolution, RTK

42

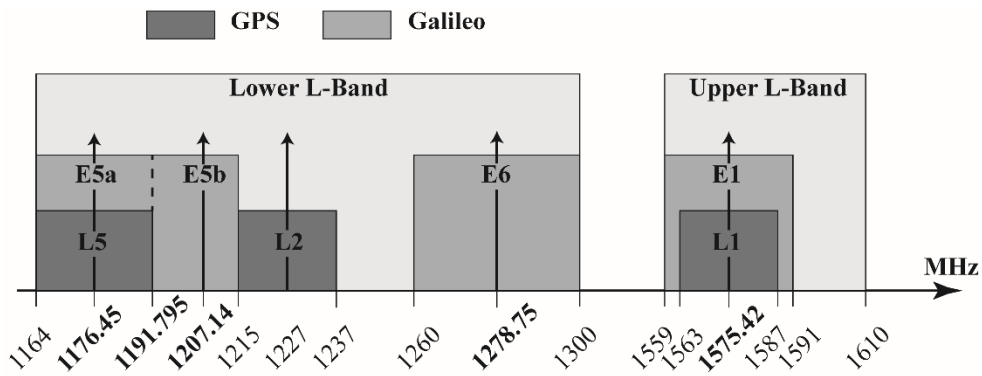
43 **Introduction**

44 Galileo, Europe's global navigation satellite system, has been under development through the
45 collaboration of the European Commission (EC) and the European Space Agency (ESA),
46 with the aim of providing highly accurate global positioning services (ESA 2016). Upon
47 validating the Galileo design, two experimental GIOVE (Galileo In-Orbit Validation
48 Element) satellites, i.e. GIOVE-A and -B, were launched in 2005 and 2008, respectively.
49 These satellites were put into orbit with the purpose of characterizing the performance of the
50 novel Galileo signals and were later on decommissioned in 2012. The last two phases of the
51 Galileo program are the IOV (In-Orbit Validation) phase and the FOC (Full Operational
52 Capability) phase. The former was planned to conduct the initial validation of the Galileo
53 system based on four satellites and became finalized by 2014, while the latter is still ongoing
54 to realize the fully-operational system such that a minimum of four satellites is always visible
55 at any location (<http://www.esa.int/>).

56 The full constellation of Galileo will comprise 24 satellites plus at most six spares,
57 expected to be realized by 2020. They orbit in three MEO (Medium Earth Orbit) planes, at an
58 altitude of 23,222 km and with an inclination angle of 56° with respect to the equator

59 (European Commission, 2015). The navigation signals of these satellites are transmitted on
 60 five frequencies E1, E5a, E5b, E5 and E6 (Table 1). Having AltBOC (Alternative Binary
 61 Offset Carrier) modulation, the Galileo E5 signal is a wideband signal consisting of two sub-
 62 carriers, i.e. E5a and E5b, which can be tracked either as two independent BPSK(10) (Binary
 63 Phase Shift Keying) modulations at respective center frequencies of 1176.45 MHz and
 64 1207.14 MHz, or coherently as one signal centered at 1191.795 MHz, leading to the E5
 65 signal (Simsy et al. 2006). Figure 1 illustrates how these frequencies are distributed with
 66 respect to the GPS L1, L2, and L5 frequencies.

67



68

69 **Fig. 1** Distribution of the Galileo frequencies versus GPS frequencies.

70

71 The first analyses of the power, tracking noise and multipath performance of the Galileo
 72 signals based on the GIOVE-A and -B data were provided in (Simsy et al. 2006, 2008a,b).
 73 Applying a geometry-free short- and zero-baseline analysis method to the measurements of
 74 GIOVE-A and -B, deBakker et al. (2009, 2012) analyzed the code and phase noise of E1 and
 75 E5a signals. Such zero-baseline analysis was also carried out by Cai et al. (2016) but on the
 76 basis of the four IOV satellites data at E1, E5a, E5b and E5 frequencies. The code noise and
 77 the cross-correlation of these frequencies were assessed in (Odijk et al. 2014).

78

79 **Table 1** Galileo frequencies and wavelengths.

Signal	Carrier frequency (MHz)	Wavelength (cm)
E1	1575.420	19.03
E5a	1176.450	25.48
E5b	1207.140	24.83

E5	1191.795	25.15
E6	1278.750	23.44

80

81 Throughout different phases of the Galileo development, its data have been studied for a
82 variety of GNSS applications either in Galileo-only mode or in Galileo plus other GNSSs
83 mode. Examples of such studies are (Langley et al. 2012; Tegedor et al. 2014, 2015; Afifi
84 and El-Rabbany 2014; Cai et al. 2015; Li et al. 2015; Lou et al. 2016; Guo et al. 2017) who
85 presented the PPP (Precise Point Positioning) results, (Odijk et al. 2012, 2014; Odolinski et
86 al. 2015) who provided the short-baseline RTK (Real-Time Kinematic) positioning results,
87 (Steigenberger et al. 2013; Cai et al. 2014; Gioia et al. 2015; Gaglione et al. 2015;
88 Steigenberger and Montenbruck 2016; Pan et al. 2017; Liu et al. 2017) who analyzed the SPP
89 (Single Point Positioning) performance, and (Nadarajah et al. 2013, 2015; Nadarajah and
90 Teunissen 2014) who provided the attitude determination results.

91 The Galileo constellation in April 2017 consists of four IOV and 14 FOC satellites. The
92 first two FOC satellites (PRNs E14 and E18) were launched in August 2014, albeit into
93 wrong orbits (Hellemans 2014). By early 2015, they were moved to an improved orbit, such
94 that the Galileo ground segment is now able to produce the navigation messages for these
95 two satellites (GSA, 2017). The fourth IOV satellite (PRN E20) experienced a power
96 anomaly on 27 May 2014, which led to the shutdown of the E1 signal. Although this signal
97 recovered within seconds, E5 and E6 signals suffered a permanent loss of power. Since then,
98 PRN E20 has been flagged as ‘NOT AVAILABLE’ (Langley 2014). Among the 14 FOC
99 satellites, four are newly-launched and not operational yet. Therefore, in total, 13 Galileo
100 satellites are currently providing data to the GNSS users. In the sequel, we refer to the
101 constellation of these 13 satellites as the current Galileo constellation.

102 We analyze the multipath performance and the noise characteristics of all the five Galileo
103 signals. For the former, the multipath combinations (Estey and Meertens 1999) are formed
104 while for the latter use is made of the least-squares variance component estimation (LS-VCE)
105 method (Teunissen and Amiri-Simkooei 2008; Amiri-Simkooei et al. 2009). These
106 assessments are on the basis of the data of the current Galileo constellation—excluding E14
107 and E18—collected by baselines of various lengths and different receiver/antenna types in
108 Perth, Australia and in the Netherlands. This is the first time that the stochastic properties of
109 the Galileo signals are assessed using both IOV and FOC satellites measurements. Our
110 outcomes, in agreement with the previous studies (Simsy et al. 2006, 2008a), show a

111 significantly lower level of noise and multipath for the E5 signal. This gives us the
 112 motivation to further investigate the E5 instantaneous RTK positioning performance. We
 113 then provide the Galileo standalone single-frequency E5-based RTK results. The
 114 understanding provided by such single-frequency analysis would also be useful for multi-
 115 frequency analysis when integrating E5 with other frequencies. The detailed information on
 116 the data used in this study can be found in Table 2. Note the antennas used in this study do
 117 not offer, at the moment, the phase center calibrations for the Galileo E5, E5a, E5b and E6
 118 signals. However, our analyses employing the short baselines of identical antennas are not
 119 affected by the lack of such calibrations (Mader 2002; EL-Hattab 2013).

120 **Table 2** Characteristics of the data set used for this study. All the antennas are survey grade
 121 and of choke-ring type.

Receiver—Firmware	Location	Station name
Antenna—Radome		
Septentrio PolaRx5—5.1.1	Curtin University,	CUBS, CUCS
TRM 59800.00—SCIS	Perth, Australia	SP01, UWA0
Leica GR50—4.00/7.001	the Netherlands	ADR2
LEIAR20+S10—LEIM		
Leica GR50—4.00/7.001	the Netherlands	APEL
LEIAR25.R4—LEIT		
Data type	Galileo E1, E5a, E5b, E5, E6 (E6 is tracked only by Septentrio PolaRx5)	
Satellites	FOC (E01,E02,E08,E09,E22,E24,E26,E30) IOV (E11,E12,E19)	
Sampling interval	1 second (1Hz)	
Baselines	CUBS-CUCS (6m) CUBS-SP01 (350m)	

122

123 Galileo Signals Characteristics

124 In this section, our aim is to characterize the Galileo signals stochastic properties. To do so,
125 we investigate their power through C/N_0 (carrier-to-noise density ratio), multipath
126 performance through the code multipath combinations, and code and phase noise by means
127 of the LS-VCE method.

128

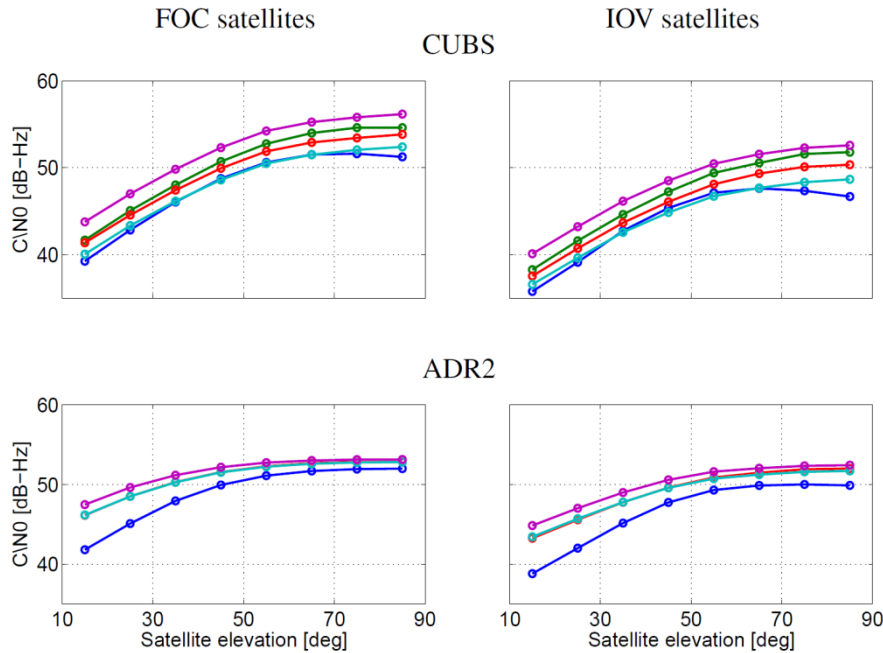
129 Signal Power

130 Shown in Figure 2 are the graphs of the carrier-to-noise density ratio C/N_0 of the Galileo
131 signals with respect to the satellites elevation. The top two panels correspond to the
132 measurements of station CUBS (Septentrio PolaRx5) while the bottom two panels
133 correspond to those of station ADR2 (Leica GR50). The ground-track of the Galileo
134 constellation, except the two FOC satellites E14 and E18, repeats every 10 sidereal days, and
135 therefore the Galileo satellites do not reach the whole range of elevations during one single
136 day. Therefore, the C/N_0 measurements were collected during a period of 10 days in 2017,
137 which are DOYs (Days Of Year) 54-63 in the case of CUBS, and DOYs 12-21 in the case of
138 ADR2. For each station, the left panel corresponds to the FOC satellites while the right panel
139 corresponds to the three IOV satellites. Each panel shows the average of the C/N_0 data over
140 elevation bins of 10 degrees. Note that E6 signal is tracked only by Septentrio PolaRx5
141 receiver.

142 Comparing the C/N_0 of Galileo signals, E5 shows the highest level of the carrier-to-noise
143 density ratio for all the elevation angles, for both the FOC and IOV satellites and for both
144 stations. In the case of CUBS, E1 and E5a have almost the same C/N_0 for the range of
145 elevations between 25 and 75 degrees. For the elevation angles out of this range, E5a reaches
146 a higher level of carrier-to-noise density ratio compared to the E1 particularly for the
147 elevations higher than 75 degrees. It can also be seen that the C/N_0 of E1 experiences a drop
148 at high elevations which was also reported in (Simsy et al. 2006) using the Space
149 Engineering antenna tracking the E1 data of GIOVE-A. The C/N_0 of E6 lies above that of
150 the E5b with almost the same difference for all the elevation angles. These two signals have a
151 higher level of C/N_0 with respect to the E1 and E5a. As to ADR2, the C/N_0 signature of E5a

152 coincides with that of E5b, both having higher levels than C/N0 of E1.

153



154

155 **Fig. 2** Carrier-to-noise density ratio C/N0 of the Galileo signals on different frequencies as
156 function of satellite elevation. The top two panels correspond to the measurements collected
157 by station CUBS during DOYs 54-63 of 2017. The bottom two panels correspond to the
158 measurements collected by station ADR2 during DOYs 12-21 of 2017. Each panel shows the
159 average of C/N0 over elevation bins of 10 degrees.

160 The observed carrier-to-noise density ratio depends on several factors such as the signal
161 path, satellite hardware and antenna, receiving equipment including receiver, antenna, splitter
162 and cable (Simsy et al. 2006; Hauschild et al. 2012). Such dependencies are well reflected
163 in our observations in Figure 2. The signals transmitted by the IOV satellites show a lower
164 level of C/N0 in comparison with their FOC counterparts. This difference probably stems
165 from the FOC and IOV satellites being different in transmit antenna patterns and transmit
166 power levels. In addition, in 2014, following the fourth IOV (E20) sudden power loss and
167 failure in transmission of the E5 and E6 signal, ESA imposed a reduction of 1.5 dB in the
168 signal power of all the four IOV satellites (Langley 2014; Steigenberger and Montenbruck,
169 2016). Beside the discrepancy between the IOV and FOC signals C/N0, we also noticed a
170 difference between the C/N0 of IOV satellite pair E11/E12 and IOV satellite E19, being
171 more pronounced in the case of Septentrio PolaRx5 receiver. According to our observations,

172 the carrier-to-noise density ratio for E19 lies below that of the other two IOV satellites for the
 173 elevations higher than 60 degrees.

174

175 Multipath performance

176 The Galileo code modulations are theoretically expected to suppress the long-delay
 177 multipath. In this sense, E5AltBOC not only outperforms the other signals, but it is also
 178 expected to have a high level of short-delay multipath rejection (Simsy et al. 2006, 2008a).
 179 In order to assess the multipath impact on Galileo signals, we form the code multipath
 180 combinations using the data collected by stations CUBS, SP01, and ADR2. The first two
 181 stations are equipped with the same receiver and antenna type, but have a different multipath
 182 environment (Table 2). The antennas deployed at all these three stations are of choke-ring
 183 type with low gain at low and negative elevation angles (Tranquilla et al. 1994). The code
 184 multipath combination is given as follows (Estey and Meertens 1999)

$$\begin{aligned}
 185 \quad \eta_{r,j}^s &= p_{r,j}^s - \varphi_{r,j}^s + 2 \frac{\lambda_j^2}{\lambda_i^2 - \lambda_j^2} (\varphi_{r,i}^s - \varphi_{r,j}^s) & (1) \\
 186 \quad &= \xi_{p_{r,j}^s} + c_{r,\{j,i\}}^s + \epsilon_{r,\{j,i\}}^s
 \end{aligned}$$

187 where $p_{r,j}^s$ and $\varphi_{r,j}^s$ denote the code and the phase observation from receiver r to satellite s on
 188 frequency j , respectively. λ_j is the wavelength of the frequency j . The code multipath
 189 combination $\eta_{r,j}^s$ is composed of code multipath, $\xi_{p_{r,j}^s}$, receiver/satellite hardware delays and
 190 integer-valued ambiguities on both frequency j and i , $c_{r,\{j,i\}}^s$, and the phase noise and
 191 multipath on both frequency j and i and the code noise on frequency j , $\epsilon_{r,\{j,i\}}^s$. The
 192 contribution of the multipath and noise of the phase observations $\varphi_{r,i}^s$ and $\varphi_{r,j}^s$ is amplified
 193 through the factor $\frac{2\lambda_j^2}{\lambda_i^2 - \lambda_j^2}$ which in case j is set to E1, E5a, E5b, E5 and E6 can, respectively,
 194 reach up to 3.9 (i: E6), 78.2 (i: E5), 77.2 (i: E5), 76.2/79.2 (i: E5a/E5b) and 16.4 (i: E5b). The
 195 significance of this contribution for a given j is then governed by the choice of i and the
 196 relative magnitude of the multipath and noise of $p_{r,j}^s$ compared to those of $\varphi_{r,i}^s$ and $\varphi_{r,j}^s$. As
 197 will be discussed in the next subsection, the multipath and noise of the code observations of
 198 E1, E5a, E5b and E6 frequencies are by far greater than those of the phase observations, such
 199 that when j is set to one of these frequencies, the contribution of the phase noise and
 200 multipath to (1) can practically be neglected for any choice of i . As to E5, however, due to

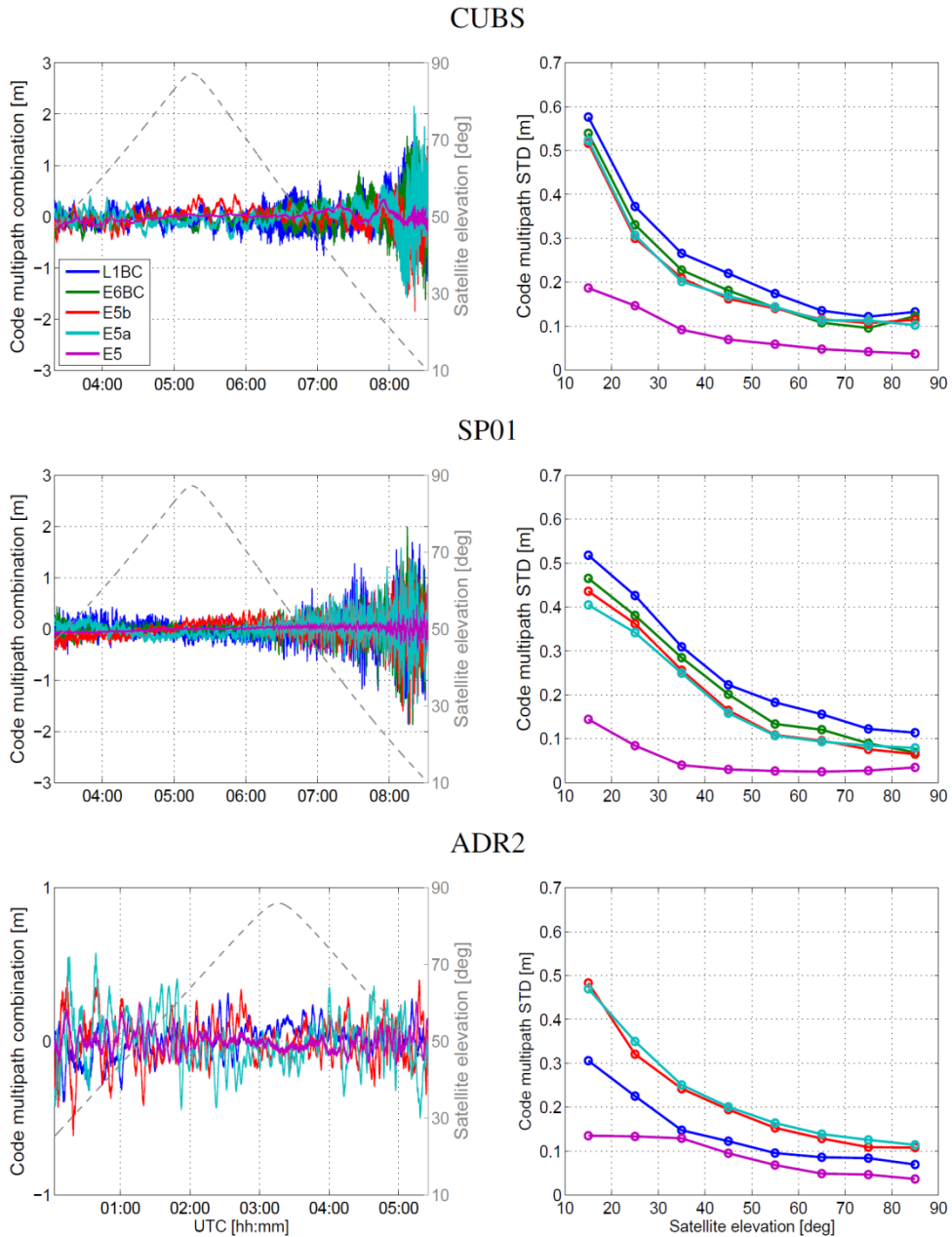
201 having centimeter-level code precision, one should avoid i: E5a/E5b since the phase noise
202 and multipath contribution to (1) would be as large as code noise and multipath. In the
203 following, for the cases j: E5a, E5b, E5 and E6, we set i: E1, and for the case j: E1, we set i:
204 E5.

205 Figure 3 (Left) depicts the time series of the code multipath combination of the Galileo
206 signals observed between station-satellite (from top to bottom) CUBS-E26 on DOY 118 of
207 2017, SP01-E26 on DOY 118 of 2017 and ADR2-E11 on DOY 21 of 2017. The satellite
208 elevation is also shown as a gray dashed line. During the considered periods, the
209 receiver/satellite hardware delays can be assumed constant over time, and since there was no
210 loss of lock, the ambiguities are also constant over time. Therefore the term $c_{r,\{j,i\}}^S$ in (1) can
211 be eliminated if the mean value of $\eta_{r,j}^S$ time series during the mentioned periods, denoted by
212 $\bar{\eta}_{r,j}^S$, is subtracted from the $\eta_{r,j}^S$ time series. Shown in Figure 3 (Left) are then the time series
213 of $\eta_{r,j}^S - \bar{\eta}_{r,j}^S$. The differences in the multipath signature between these three panels stem from
214 the differences in multipath environment and, in case of the right panel, the receiver/antenna
215 type. As the satellite elevation decreases, the code multipath fluctuates more rapidly and with
216 higher amplitudes. The Galileo signals in terms of the severity of this behavior can be
217 ordered as E1>E5a>E5b>E6>E5 for the stations CUBS and SP01, and as E5a>E5b>E1>E5
218 for the station ADR2. As to the E5, this behavior is mitigated considerably such that the E5
219 code multipath can be assumed to a large extent independent of the satellite elevation. The
220 high performance of the E5 signal lies in its wide bandwidth and AltBOC modulation
221 (Simsky et al. 2006; Diessongo et al. 2014).

222 Figure 3 (Right) provides the standard deviation of the code multipath combination over
223 elevation bins of 10 degrees for the Galileo signals. These graphs are obtained based on all
224 the Galileo observations recorded by the corresponding stations during 10 days. The
225 multipath performance of three signals E5a, E5b and E6 are similar to each other, poorer than
226 E1 in the case of station ADR2 and better than E1 in the case of stations CUBS and SP01.
227 The graphs corresponding with E5AltBOC shows a much flatter signature, revealing a small
228 difference between high-elevation and low-elevation multipath for this signal. This
229 observation is also consistent with the results presented by Simsky et al. (2006) based on the
230 observations of GIOVE-A.

231

232



233

234

235 **Fig. 3** Galileo code multipath behavior. (Left) Code multipath combination time series based
 236 on the observations of station-satellite (from top to bottom) CUBS-E26 on DOY 118 of
 237 2017, SP01-E26 on DOY 118 of 2017 and ADR2-E11 on DOY 21 of 2017. The satellite
 238 elevation is indicated by the dashed line. (Right) The standard deviation of the code
 239 multipath combination over elevation bins of 10 degrees, based on all the Galileo
 240 observations recorded by (from top to bottom) station CUBS and SP01 during DOYs 118-
 241 127 of 2017 and station ADR2 during DOYs 12-21 of 2017.

242

243 Measurement noise

244 The GNSS underlying observational model consists of two parts: functional model and
245 stochastic model. The former describes how the parameters of interest, e.g. receiver-satellite
246 range, ionospheric delay, receiver clock error, are related to the GNSS observations, while
247 the latter describes the noise characteristics of the GNSS observables. In order to assess the
248 noise characteristics of the Galileo signals, we employ the Galileo data of the short baselines
249 CUBS-CUCS, CUBS-SP01, ADR2-APEL, and CUBS-UWA0 (Table 2), for which the
250 differential ionospheric and tropospheric delays can be assumed negligible. With the
251 covariance $C(\cdot, \cdot)$ operator, we consider the following stochastic model for the undifferenced
252 code and phase observations on frequency j ,

$$253 \quad C(p_{r,j}^s, p_{u,j}^v) = \delta_{ru} \delta_{sv} \sigma_{p_j}^2 w^s, \quad C(\varphi_{r,j}^s, \varphi_{u,j}^v) = \delta_{ru} \delta_{sv} \sigma_{\varphi_j}^2 w^s, \quad C(p_{r,j}^s, \varphi_{u,j}^v) = 0 \quad (2)$$

254 where δ_{ru} is the Kronecker delta ($\delta_{ru} = 1$ for $r = u$ and zero otherwise), and δ_{sv} is defined
255 likewise. w^s captures the satellite-elevation dependency of the Galileo data through the
256 exponential weighting function as

$$257 \quad w^s = \left(1 + 10 \exp\left(-\frac{\theta^s}{10}\right)\right)^{-2} \quad (3)$$

258 where θ^s is the elevation of satellite s in degrees (Euler and Goad 1991). Note we have
259 dropped the receiver index from θ^s and w^s since the elevation of satellite s can be assumed
260 the same for the considered station pairs which are separated at a short distance. σ_{p_j} and σ_{φ_j}
261 denote the zenith-referenced standard deviations of the undifferenced code and phase
262 observations on frequency j , respectively.

263 Our aim is to find representative values for $\{\sigma_{p_j}, \sigma_{\varphi_j}\}$ ($j = 1, \dots, 5$). To do so, we apply the
264 LS-VCE method (Teunissen and Amiri-Simkooei 2008; Amiri-Simkooei et al. 2009) to the
265 1-second (1Hz) double-differenced (DD) code and phase observations which are corrected
266 for the DD ranges and, in case of phase observations, the integer DD ambiguities. The DD
267 ranges were computed from the known receiver and satellite positions. Whereas the reference
268 integer ambiguities were computed using the very strong multi-epoch baseline-known model
269 in which the observations of multiple epochs are incorporated, the ambiguities are assumed
270 to be constant over time and the baseline components are assumed known. These corrected
271 DD observations and the so estimated variances, will capture the combined effect of the
272 transmitted signal quality, the receiver architecture like correlator and loops, as well as any

273 remaining mis-modeled effects like multipath. The impact of multipath can be largely
274 mitigated through the method explained in the following. Since the stations in use are static
275 and their surrounding environment almost remains unchanged over time, the multipath
276 influence on a signal of a specific frequency is expected to repeat when the Galileo receiver-
277 satellite geometry repeats after 10 sidereal days. Therefore by subtracting the corrected DD
278 observations corresponding with the same satellite geometry (obtained every 10 sidereal
279 days), the adverse multipath impact can be largely eliminated (Bock 1991; Genrich and Bock
280 1992; Zaminpardaz et al. 2016).

281 Table 3 lists the estimated standard deviations of the Galileo code σ_{p_j} and phase σ_{φ_j}
282 observations with and without multipath corrections. For static stations, as used in this study,
283 the multipath pattern for the Galileo constellation is expected to repeat every 10 sidereal
284 days. This indicates that for every 10-day period, the multipath signature differs from day to
285 day. Therefore, the standard deviations estimations of the original observations in Table 3 are
286 obtained based on 10-day data sets. Prior to applying the multipath corrections to these data
287 sets using the data of 10 days later as explained above, we first checked whether the
288 multipath pattern indeed repeats after 10 sidereal days. Our observations showed that, in spite
289 of the multipath environment remaining unchanged over time, for some of the satellites
290 during some time intervals the multipath signature does not show a good repeatability. As an
291 example, Figure 4 for the station-satellite CUBS-E12 shows the E1 code multipath
292 combination time series during a 48-minute period on DOY pairs (blue-red) 123-133 (top)
293 and 124-134 (bottom). The satellite elevations during the considered periods in top and
294 bottom panels are similar. The UTC labels given in the top/bottom panel are on DOY
295 133/134, and therefore the UTC for the blue graphs are obtained by adding 2420 seconds
296 ($\approx 10 \times$ four minutes) to the shown UTC labels. It can be seen that while the multipath pattern
297 shows consistent signature for DOY pair 123-133, its behavior differs from DOY 124 to
298 DOY 134. A possible explanation for this discrepancy is as follows. The time shift that we
299 use for DOY pairs 123-133 and 124-134 is 2420 seconds which has been computed through
300 cross-correlation of the corresponding baseline (CUBS-CUCS) estimation time series on
301 DOYs 53 and 63 of 2017. However, our observations show that the repeat cycle varies
302 among different Galileo satellites. Even for a given specific satellite, the repeat cycle changes
303 from time to time. Any variation in the satellite geometry would then result in the variation in
304 multipath signature. Thus, for estimating the multipath-corrected standard deviations in Table
305 3, we only chose data of those days showing very similar multipath signature to that of their

306 counterparts 10 days later, with the purpose of providing values one could achieve in case the
 307 multipath could have been eliminated. Note for multipath-corrected estimations, due to day-
 308 differencing, we have taken the doubling of the noise level into account through replacing w^S
 309 by $2w^S$.

310

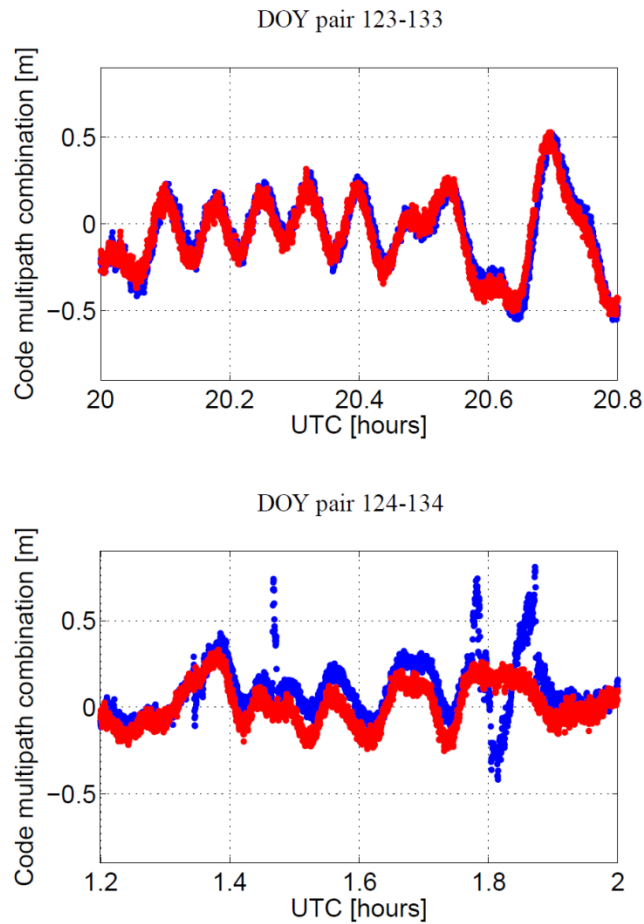
311 **Table 3** LS-VCE estimation of the undifferenced code σ_p and phase σ_ϕ zenith-referenced
 312 standard deviations of the Galileo data. For each frequency and each baseline, two values are
 313 given for σ_p and σ_ϕ which, from left to right, correspond to the original and multipath-
 314 corrected data.

	Signal	CUBS-CUCS	CUBS-SP01	ADR2-APEL	CUBS-UWA0
σ_p (cm)	E1	21.2,10.8	18.9, 9.8	17.5, 3.2	16.4, 9.8
	E5a	15.3, 5.6	14.9, 5.5	19.6, 3.7	13.7, 5.5
	E5b	16.3, 5.6	15.1, 5.6	18.8, 3.7	14.1, 5.6
	E5	6.4, 1.1	5.1, 1.1	6.8, 1.0	5.1, 1.2
	E6	16.5, 7.5	16.6, 7.6	-- , --	13.1, 7.9
σ_ϕ (mm)	E1	1.4, 0.5	3.0, 0.8	3.8, 0.9	5.7, 3.2
	E5a	1.5, 0.5	3.1, 0.9	3.8, 1.3	6.8, 4.5
	E5b	1.4, 0.5	3.1, 0.8	3.6, 1.3	6.7, 4.4
	E5	1.1, 0.4	3.0, 0.8	3.6, 1.3	6.7, 4.4
	E6	1.4, 0.5	3.0, 0.8	-- , --	5.6, 4.1

315

316 Despite having the same receiver and antenna type, baselines CUBS-CUCS, CUBS-SP01
 317 and CUBS-UWA0 show differences in their estimations of the original data standard
 318 deviations which can be attributed to the differences in the multipath environment of the
 319 stations CUCS, SP01 and UWA0. These discrepancies would vanish though, were the
 320 multipath effect be completely eliminated. This is also confirmed comparing the
 321 corresponding outcomes based on the original and multipath-corrected data. It can be seen
 322 that upon applying multipath corrections, the differences between the estimations of the
 323 mentioned three baselines get smaller. The stations forming the baseline ADR2-APEL have
 324 different antenna types (Table 2). The results presented in Table 3 for this station pair thus
 325 capture the combined effect of different antenna types involved. Comparing the standard

326 deviation estimations of a specific signal based on the data of different baselines, one notes
 327 that the ordering would change if the multipath corrections are applied. For example, the
 328 code precision of the E5a original data improves from ADR2-APEL to CUBS-CUCS to
 329 CUBS-SP01 to CUBS-UWA0, whereas on the basis of E5a multipath-corrected data, the
 330 code precision improves from CUBS-CUCS to CUBS-SP01/CUBS-UWA0 to ADR2-APEL.



331

332 **Fig. 4** Code multipath combination time series based on the E1 observations of station-
 333 satellite CUBS-E12 on (Top) DOYs 123 (blue) and 133 (red) of 2017 (Bottom) DOYs 124
 334 (blue) and 134 (red) of 2017.

335

336 The order in which the signals can be arranged in terms of their precision is different for
 337 various receiver/antenna types. The code standard deviation of the E5 signal, however, shows
 338 lower dependency on the receiver/antenna type and the multipath environment, and
 339 significantly smaller values with respect to that of the other signals. Upon applying the
 340 multipath correction, the code standard deviations of all the signals experience a dramatic
 341 reduction which is a factor of five in the case of E5. The phase precision estimations either

342 with or without multipath corrections, in contrast to their code counterparts, do not show any
343 dependency on the signal type.

344 The results presented in Table 3 have been obtained combining the observations of the
345 IOV and FOC satellites. We also carried out the LS-VCE estimations based on the IOV-only
346 and FOC-only observations. The estimated code standard deviations of the FOC satellites are
347 generally smaller than those of the IOV satellites. The phase observations of these two types
348 of satellites, however, show similar precisions.

349

350 **E5AltBOC RTK Analysis**

351 It was shown in the previous section that among the five Galileo signals, E5AltBOC shows a
352 significantly higher signal power and lower level of multipath and noise. Such characteristics
353 give us the motivation to further analyze the high-performance E5 signal for its potential
354 capability in RTK positioning. In this section, we present the results of the Galileo E5-based
355 instantaneous RTK performance. Our assessments are carried out based on the Galileo data
356 collected by CUBS-CUCS (6-day data set; DOYs 54, 56-60 of 2017), CUBS-SP01 (5-day
357 data set; DOYs 123-127 of 2017), ADR2-APEL (1-day data set; DOY 17 of 2017) and
358 CUBS-UWA0 (2-day data set; DOYs 173-174 of 2017), once without multipath correction
359 and once with multipath correction provided by the Galileo data 10 days later. With the
360 current Galileo constellation, there exist time intervals with less than four visible satellites,
361 accounting for 41% and 51% of a repeat cycle of 10 days at Perth and the Netherlands,
362 respectively. These percentages increase further to 78% upon excluding E14 and E18, which
363 is the case with our analyses in this contribution. The periods considered for our RTK
364 evaluations accommodate time intervals with four to five visible satellites. In case of the first
365 two baselines, there is a very short time interval with six satellites being visible. Given the
366 limited number of visible Galileo satellites, the corresponding PDOP (Position Dilution Of
367 Precision) reaches extremely large values, thus making positioning almost infeasible. In
368 order to leave out these extreme values, in the sequel, we consider various PDOP thresholds
369 when presenting RTK results.

370

371 **GNSS single-frequency observational model**

372 Let us assume that two receivers are simultaneously tracking m Galileo satellites on a single
373 frequency, say E5. The corresponding multivariate DD observation equations can be cast in

374 (Teunissen and Montenbruck 2017, Chap. 1; Hofmann-Wellenhof et al. 2008, Chap. 5)

$$375 \quad E \begin{bmatrix} D_m^T p \\ D_m^T \varphi \end{bmatrix} = \begin{bmatrix} D_m^T G & 0 \\ D_m^T G & \lambda I_{m-1} \end{bmatrix} \begin{bmatrix} b \\ a \end{bmatrix}$$

376 (4)

$$377 \quad D \begin{bmatrix} D_m^T p \\ D_m^T \varphi \end{bmatrix} = \begin{bmatrix} \sigma_p^2 Q & 0 \\ 0 & \sigma_\varphi^2 Q \end{bmatrix}$$

378 where $E[\cdot]$ and $D[\cdot]$ denote, respectively, the expectation and dispersion operator. The
 379 observations are formed by the vectors of the DD code and phase measurements, obtained by
 380 applying the between-satellite differencing operator D_m^T to the m -vector of between-receiver
 381 single-differenced (SD) code p and phase φ measurements. The $(m-1) \times m$ differencing
 382 operator can be formed as e.g. $D_m^T = [-e_{m-1}, I_{m-1}]$ where e_{m-1} and I_{m-1} denote the
 383 vector of ones and the identity matrix, respectively. The unknowns to be estimated are the 3-
 384 vector of the baseline increments b , linked to the observations through the $m \times 3$ geometry
 385 matrix G , and the $(m-1)$ -vector of the DD ambiguities a , linked to the phase observations
 386 through the signal wavelength λ . The noise of the measurements is characterized through
 387 three factors, i.e. σ_p, σ_φ and $Q = D_m^T W^{-1} D_m$. σ_p and σ_φ denote the zenith-referenced
 388 standard deviation of the undifferenced code and phase measurements (cf. 2), and W is the
 389 $m \times m$ diagonal matrix having the satellite elevation-dependent weights w^s (cf. 3) as its
 390 diagonal entries. Note our analyses are based on the short-baseline data where the differential
 391 ionospheric and tropospheric delays can be neglected.

392 As (4) suggests, for the single-epoch analyses, the phase observations are fully reserved
 393 for the estimation of the DD ambiguities. The estimation of the baseline would then be
 394 governed by the code observations only. The so obtained solutions for the baseline and the
 395 DD ambiguities are called float solutions. Upon resolving the DD ambiguities to their integer
 396 values, the phase observations would take the leading role in the baseline estimation. The so
 397 obtained solutions for the baseline and the DD ambiguities are called fixed solutions.

398

399 Ambiguity resolution results

400 Successful phase ambiguity resolution is a prerequisite to the realization of RTK positioning.
 401 As a measure to analyze the Galileo E5 ambiguity resolution performance in the framework
 402 of the model given in (4), we make use of the integer bootstrapped (IB) success rate as it is

403 easy to compute, and also the sharpest lower bound to the integer least-squares (ILS) success
 404 rate which has the highest success rate of all admissible integer estimators (Teunissen 1999;
 405 Verhagen and Teunissen 2014). The formal IB success rate is computed as (Teunissen 1998)

$$406 \quad \text{Formal IB Ps} = \prod_{i=1}^{m-1} \left[2\Phi\left(\frac{1}{2\sigma_{z_{i|I}}}\right) - 1 \right] \quad (5)$$

407 with $\Phi(x) = \int_{-\infty}^x \frac{1}{\sqrt{2\pi}} \exp\left\{-\frac{1}{2}v^2\right\} dv$ and $\sigma_{z_{i|I}}$ ($i = 1, \dots, m - 1$ and $I = 1, \dots, i - 1$) being the
 408 conditional standard deviations of the decorrelated ambiguities. As the formal IB success rate
 409 is model-driven, to check the consistency between our data and the assumed underlying
 410 model, we also compute the empirical IB success rate which is data-driven and given as

$$411 \quad \text{Empirical IB Ps} = \frac{\# \text{ correct fixed DD ambiguities}}{\# \text{ float DD ambiguities}} \quad (6)$$

412 To judge whether a float DD ambiguity (\hat{a}) is correctly fixed, its corresponding IB solution
 413 (\check{a}) is compared with the reference integer DD ambiguity (a) computed based on the multi-
 414 epoch ILS solution of the baseline-known model. Table 4 shows the empirical and formal
 415 single-epoch IB success rates for both the original and multipath-corrected data of the
 416 mentioned four baselines. The formal values in this table are obtained through averaging the
 417 formal IB success rates over the period in use. In addition, since for the positioning results,
 418 coming in the next subsection, we consider various thresholds for PDOP value, we apply
 419 them here as well. One should, nevertheless, have in mind that the ambiguity resolution
 420 performance is not characterized through PDOP (Zaminpardaz et al. 2016, p. 546).

421 The results in Table 4 state that upon applying the multipath corrections, the IB success
 422 rates increase dramatically such that (almost) instantaneous ambiguity resolution becomes
 423 feasible. For example, if an ambiguity resolution success rate of 99.9% is sought for RTK
 424 positioning, our computation shows that, on average, four epochs of 1-second data are
 425 required. However, there still remains some inconsistencies between empirical and formal
 426 outcomes which can be attributed to the existence of the multipath residuals as explained in
 427 the following. As was mentioned previously, applying the multipath corrections cannot fully
 428 eliminate the multipath impact on our data sets, thereby leaving some residuals. The
 429 multipath-corrected standard deviations in Table 3, based on which the multipath-corrected
 430 formal success rates are computed, also, in turn, capture the impact of the multipath residuals
 431 of the underlying data sets. The multipath-corrected empirical success rates in Table 4 are
 432 also affected by the multipath residuals of the corresponding data sets. The difference of the

433 multipath residuals existing in the data sets used in Table 3 and those employed in Table 4, if
 434 non-negligible, can lead to disagreement between empirical and formal success rates. Note
 435 that the differences between the formal success rates of different baselines stem from the
 436 differences in the corresponding code/phase standard deviation (Table 3) and the satellite
 437 geometry.

438

439 **Table 4** Average single-epoch formal and empirical bootstrapped (IB) success rate (%), for
 440 the original and the multipath-corrected Galileo E5 data, collected by several baselines with
 441 the cut-off elevation of 10° . For each baseline and each PDOP threshold, two rows of values
 442 are given; the first row corresponds to original data while the second row corresponds to the
 443 multipath-corrected data. emp: empirical; form: formal.

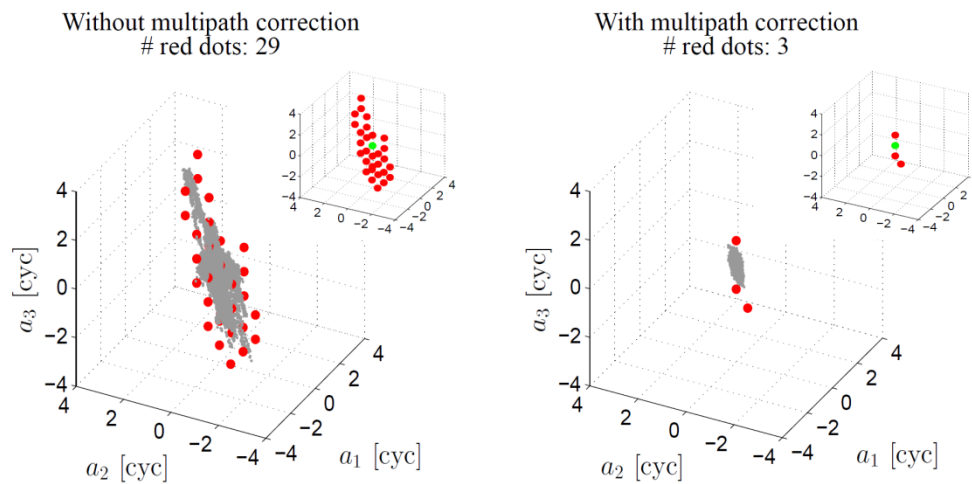
Baseline	PDOP<30		PDOP<20		PDOP<10	
	emp	form	emp	form	emp	form
CUBS-CUCS	32.2	28.0	33.1	28.5	40.2	34.6
	95.2	92.1	95.5	92.3	97.6	95.0
CUBS-SP01	32.1	27.0	33.1	27.9	30.4	26.9
	89.6	93.0	89.7	93.4	87.3	94.2
ADR2-APEL	23.2	19.9	20.9	19.5	14.1	13.6
	95.6	93.7	95.2	93.7	96.9	91.0
CUBS-UWA0	29.3	29.5	29.2	29.8	27.0	29.4
	85.1	91.4	85.1	91.9	81.4	91.4

444

445 Now, through visualization, we elaborate more on how applying the multipath correction
 446 improves the ambiguity resolution performance. For this purpose, we choose a period of
 447 7000 seconds of the CUBS-CUCS data set, over which four Galileo satellites are visible from
 448 these stations, which in turn, results in three DD ambiguities. During this period, there was
 449 no loss of lock, and therefore the DD ambiguities remained constant. Figure 5 shows the
 450 corresponding 3-dimensional scatter plot of the single-epoch solutions of $\hat{a} - a$ (gray) and
 451 $\check{a} - a$ (green: correctly fixed; red: wrongly fixed). While the left panel depicts the

452 estimations based on the original data, the right panel shows those based on the multipath-
 453 corrected data. It can be seen that once the multipath corrections are applied to our data, the
 454 scatter plot of $\hat{a} - a$ shrinks considerably, and the number of incorrectly fixed solutions
 455 decreases from 29 to 3.

456



457

458 **Fig. 5** 3-dimensional scatter plot of the single-epoch DD ambiguities in float mode $\hat{a} - a$
 459 (gray) and fixed mode $\check{a} - a$ (green: correctly fixed; red: incorrectly fixed), corresponding
 460 with the Galileo E5 data collected by CUBS-CUCS over a period of 7000 seconds on DOY
 461 54 of 2017. Given on top of each panel is the number of integers which were incorrectly
 462 determined by the IB estimator to be the DD ambiguities solution. Also, in the upper right of
 463 each panel, the scatter plot of only the fixed solutions is depicted. (Left) Without multipath
 464 correction; (Right) With multipath correction.

465

466 RTK Positioning Results

467 In this subsection, we discuss the single-epoch baseline estimation results based on the
 468 Galileo E5 observations. Setting the thresholds of 30, 20 and 10 for PDOP, Table 5 gives the
 469 empirical and formal single-epoch standard deviations of the estimated components of the
 470 baselines CUBS-CUCS, CUBS-SP01, ADR2-APEL, and CUBS-UWA0. The first two rows
 471 for each baseline give the ambiguity-float results on the basis of original and multipath-
 472 corrected data, respectively. The multipath-corrected results in Table 5 can be considered of
 473 practical relevance for kinematic users in a low multipath environment or for static baselines
 474 like e.g. for deformation monitoring. As was shown in the previous subsection, the
 475 multipath-corrected Galileo E5 data can provide (almost) instantaneous successful ambiguity

476 resolution. Therefore, the third row for each baseline gives the multipath-corrected
477 ambiguity-fixed results, which are computed based on only the correctly-fixed solutions. The
478 formal and empirical standard deviations are computed on the basis of the respective formal
479 and empirical variance matrix. The Formal variance matrix is obtained from taking the
480 average of all the single-epoch least-squares baseline variance matrices, whereas the
481 empirical variance matrix is obtained from the differences of the estimates and the available
482 ground truth of the mentioned baselines. Comparing the ambiguity-float results from the
483 original data with those from the multipath-corrected data, the precision improvement
484 achieved upon applying the multipath correction is a factor of about 4.24 which is the ratio of
485 σ_p of the original data to $\sqrt{2} \times \sigma_p$ of the multipath-corrected data. The empirical results show
486 consistency with the formal outcomes, particularly in case of the ambiguity-fixed scenario.
487 Also, the positioning precisions depend on the receiver/antenna type as well as the extent to
488 which the multipath impact can be mitigated (Table 3).

489 In the following, the positioning results of the baseline CUBS-CUCS are visualized and
490 further discussed. Shown in Figure 6 are the scatter plot of the CUBS-CUCS baseline
491 horizontal components estimation errors (top) and the time series of the baseline height
492 estimation error (bottom). Note, in this figure, we have stacked all the periods on DOYs 54
493 and 56-60 of 2017, during which a minimum of four Galileo satellites are visible, and the
494 corresponding PDOP is less than 30. The estimation errors are computed by subtracting the
495 baseline ground truth from the baseline single-epoch estimations. Different colors in this
496 figure have the following meanings; gray: float solution, green: correctly-fixed solution, and
497 red: incorrectly-fixed solution. The two left panels are based on the original data, whereas the
498 two right panels correspond with the multipath-corrected data. In the lower right panel is also
499 shown the 95% formal confidence interval (blue lines) based on the float height standard
500 deviation. To obtain these results, a threshold of 30 was imposed on the PDOP.

501 In Figure 6, the scatter plots do not show an ellipsoidal shape which is due to the
502 significant changes that the receiver-satellite geometry undergoes during the mentioned six
503 days. It can also be seen that the variation of the float solutions (gray) significantly decreases
504 upon applying the multipath correction. This is due to the improvement of the E5 code
505 precision following the elimination of the multipath effect from the code data (Table 3). The
506 density of the red and green dots can be explained by means of the formal IB success rate.
507 Figure 7 shows a zoom-in of the multipath-corrected height estimation error time series
508 between (50000, 70000) (top) and the corresponding time series of the single-epoch formal

509 IB success rate (bottom). The distribution of the red and green dots is in good agreement with
 510 the behavior of the formal IB success rate. When the success rate gets smaller, the density of
 511 red dots increases and vice versa.

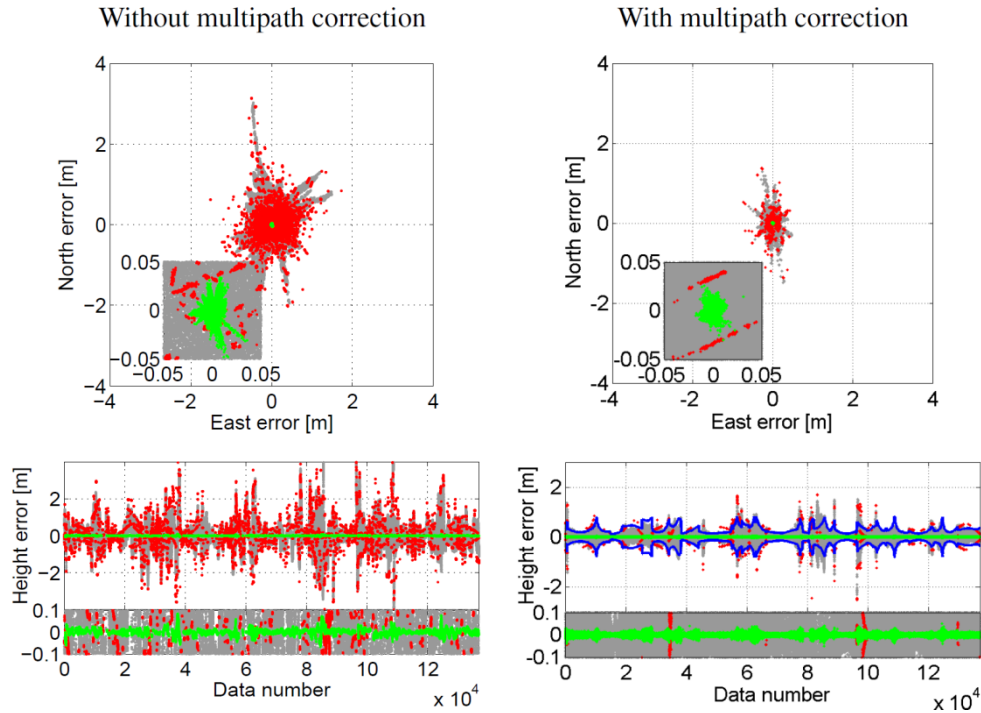
512 **Table 5** Single-epoch standard deviations of the estimated components of the baselines
 513 CUBS-CUCS, CUBS-SP01, ADR2-APEL and CUBS-UWA0 based on the Galileo E5
 514 measurements collected with the cut-off angle of 10°. For each baseline and each PDOP
 515 threshold, six values per coordinate components are given on three rows. The first row
 516 contains the ambiguity-float results without multipath correction; the second contains the
 517 multipath-corrected ambiguity-float results and the third contains the multipath-corrected
 518 ambiguity-fixed results. On each row, from left to right, empirical and formal values are
 519 presented

Baseline	PDOP<30			PDOP<20			PDOP<10		
	North	East	Height	North	East	Height	North	East	Height
CUBS-CUCS	0.268,	0.225,	0.735,	0.235,	0.213,	0.593,	0.150,	0.185,	0.412,
	0.305	0.262	0.804	0.268	0.238	0.656	0.165	0.179	0.423
	0.064,	0.044,	0.170,	0.053,	0.040,	0.143,	0.030,	0.034,	0.083,
	0.076	0.065	0.201	0.067	0.059	0.164	0.041	0.045	0.106
	0.002,	0.002,	0.006,	0.002,	0.002,	0.005,	0.001,	0.002,	0.003,
	0.003	0.002	0.007	0.002	0.002	0.006	0.001	0.002	0.004
CUBS-SP01	0.233,	0.197,	0.607,	0.200,	0.181,	0.505,	0.172,	0.165,	0.376,
	0.260	0.217	0.662	0.226	0.191	0.534	0.168	0.145	0.339
	0.085,	0.071,	0.196,	0.077,	0.066,	0.158,	0.060,	0.060,	0.134,
	0.077	0.064	0.196	0.067	0.056	0.158	0.050	0.043	0.100
	0.006,	0.005,	0.016,	0.004,	0.004,	0.012,	0.004,	0.003,	0.008,
	0.006	0.005	0.015	0.005	0.004	0.012	0.004	0.003	0.008
ADR2-APEL	0.386,	0.226,	0.746,	0.397,	0.224,	0.715,	0.252,	0.225,	0.346,
	0.387	0.260	0.799	0.378	0.248	0.690	0.305	0.205	0.503
	0.062,	0.051,	0.162,	0.062,	0.046,	0.143,	0.045,	0.035,	0.086,
	0.081	0.054	0.167	0.079	0.052	0.144	0.063	0.043	0.105
	0.011,	0.006,	0.024,	0.010,	0.005,	0.019,	0.007,	0.003,	0.012,
	0.010	0.007	0.022	0.010	0.006	0.019	0.008	0.005	0.014
CUBS-UWA0	0.229,	0.153,	0.614,	0.197,	0.143,	0.562,	0.166,	0.126,	0.364,
	0.258	0.170	0.577	0.224	0.156	0.511	0.171	0.138	0.368
	0.071,	0.053,	0.180,	0.065,	0.050,	0.166,	0.052,	0.049,	0.125,
	0.087	0.058	0.195	0.076	0.053	0.173	0.058	0.047	0.124

0.029,	0.020,	0.070,	0.024,	0.018,	0.062,	0.017,	0.016,	0.050,
0.029	0.019	0.067	0.025	0.017	0.060	0.020	0.015	0.040

520

521



522

523 **Fig. 6** CUBS-CUCS baseline solutions based on the Galileo E5 measurements collected on
 524 DOYs 54 and 56-60 of 2017 with the cut-off angle of 10° . These solutions correspond to
 525 PDOP values smaller than 30. (Top) Horizontal scatter plot with a zoom-in in the lower left.
 526 (Bottom) Height estimation errors time series with a zoom-in in the bottom. gray: float
 527 solutions; green: correctly-fixed solutions; red: incorrectly-fixed solutions. The blue lines in
 528 the lower right panel indicate the 95% formal confidence interval.

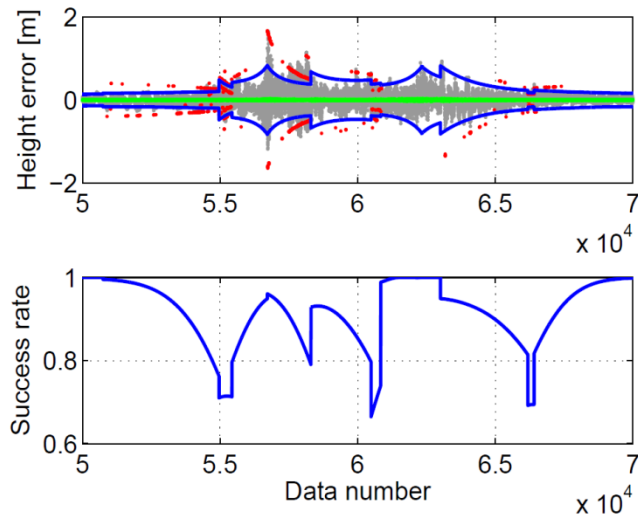
529

530 The time series of the multipath-corrected height estimation errors, except for some
 531 intervals, shows a consistent signature with its formal counterpart (blue lines). The
 532 inconsistencies between the formal and empirical float solutions can be attributed to the fact
 533 that the multipath corrections that we apply to our data cannot eliminate the multipath effect
 534 completely. Instead, they capture largely the multipath trend (low-frequency multipath
 535 components) and partly the high-frequency multipath components which are of higher
 536 amplitudes in the satellite signals received at low elevations (Figure 3, left).

537

538

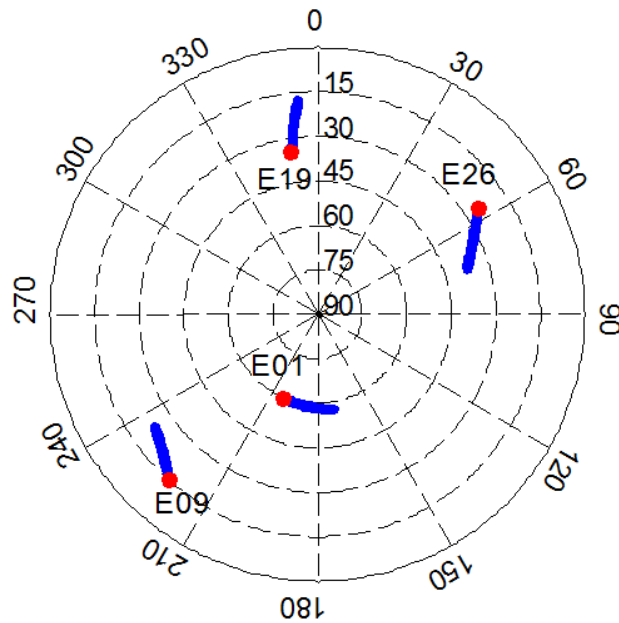
539



540

541

542 **Fig. 7** Ambiguity resolution performance. (Top) A zoom-in of the height estimation errors
543 time series illustrated in the lower right panel of Figure 6. (Bottom) The corresponding time
544 series of the single-epoch formal IB success rate.



545

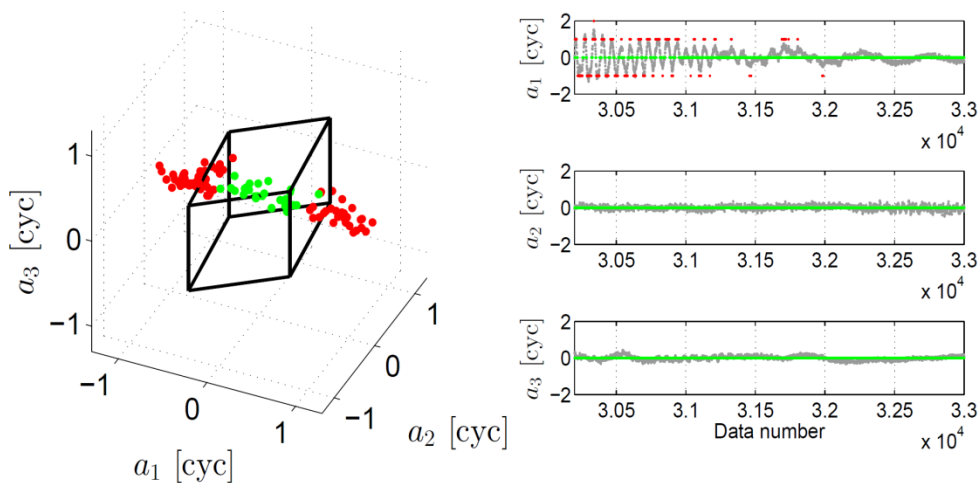
546

547 **Fig. 8** Skyplot of Galileo at Perth, Australia, during UTC(18:35:11-19:21:51) on DOY 56 of
548 2017 with a cut-off elevation of 10°. The red dots show the location of the visible satellites at
549 the first epoch of this time interval.

550

551

552 Looking at the ambiguity-fixed solutions presented in the right panel of Figure 6, during
 553 some time interval, different clusters of fixed solutions can be recognized, indicating that the
 554 DD ambiguities are resolved to different integer vectors during these periods. As an example,
 555 we consider the interval (30200 , 33000) through which there exist three (two red and one
 556 green) clusters of fixed solutions, thus three different integer estimations of the ambiguities.
 557 Shown in Figure 8 is the skyplot of the Galileo satellites at Perth during this period.
 558 According to this figure, four satellites are visible among which satellite E09 is just rising
 559 from the elevation of 15°. Figure 9 (right) shows the time series of the float and fixed DD
 560 ambiguities over the mentioned period, from top to bottom, for the satellite pairs E01-E09,
 561 E01-E19, and E01-E26, respectively. It can be seen that while the DD ambiguities of E01-
 562 E19 and E01-E26 are correctly fixed to 0, those corresponding with E01-E09 are varying
 563 between -1, 0 and 1 which is obviously due to the residuals of the high-frequency multipath
 564 components. Figure 9 (left) shows the 3-dimensional scatter plot of the float DD ambiguities
 565 during the first 100 epochs of the interval (30200, 33000), where a_1 : E01-E09, a_2 : E01-E19
 566 and a_3 : E01-E26. The zero IB pull-in region (black parallelepiped), computed based on the
 567 average DD ambiguities variance matrix over the mentioned 100 epochs, is also illustrated in
 568 this figure. The ambiguities solutions inside the pull-in region are indicated by the green dots
 569 and those outside the pull-in region by the red dots. It can be seen that the scatter plot of the
 570 DD ambiguities deviates from the zero IB pull-in region along a_1 direction, corresponding
 571 with E01-E09.



572

573

574 **Fig. 9** (Left) 3-dimensional scatter plot of the float DD ambiguities corresponding with the
575 satellite geometry shown in Figure 8 during the interval (30200 , 30300). The black
576 parallelepiped is the IB pull-in region. The float DD ambiguities inside the IB pull-in regions
577 are denoted by green dots and those outside the IB pull-in region by red dots. a_1 : E01-E09,
578 a_2 : E01-E19 and a_3 : E01-E26. (Right) Time series of the float and fixed DD ambiguities
579 over the mentioned interval. gray: float solutions; green: correctly-fixed solutions; red:
580 incorrectly-fixed solutions.

581

582 **Summary and Conclusion**

583 We provided the results of the Galileo signals stochastic properties employing 1-second data
584 collected by four short baselines of different lengths and receiver/antenna types. The
585 assessments included the observations of both the IOV and FOC satellites in the constellation
586 in April 2017 excluding E14 and E18. We analyzed the signal power, multipath performance
587 and the noise level of the Galileo E1, E5a, E5b, E5 and E6 signals. The carrier-to-noise
588 density ratio C/N0 measurements of the Galileo FOC satellites demonstrated higher values
589 than those of the IOV satellites. This can be attributed to different transmit antenna patterns
590 and transmit power levels of these two types of satellites, and also the signal power reduction
591 of all the IOV satellites imposed by ESA in 2014. For two types of receiver/antenna in use,
592 i.e. Septentrio PolaRx5/TRM 59800.00 SCIS (CUBS) and Leica GR50/LEI AR20 (ADR2),
593 our C/N0 observations revealed the following ordering $E5 > E6 > E5b > E5a \approx E1$ and
594 $E5 > E5b \approx E5a > E1$, respectively.

595 To analyze the multipath performance of the Galileo signals, the corresponding code
596 multipath combinations were formed based on the observations of three stations (CUBS and
597 SP01 at Perth and ADR2 in the Netherlands) with different multipath environment and
598 receiver/antenna type. The standard deviations of the code multipath combination as a
599 function of satellite elevation were illustrated. The multipath performance of three signals
600 E5a, E5b and E6 were similar to each other, poorer than E1 in the case of station ADR2 and
601 better than E1 in the case of stations CUBS and SP01. A strong satellite-elevation
602 dependency was visible in the code multipath of all these four signals. Taking considerably
603 smaller values, E5 signal multipath showed a weak dependency on the satellite elevation.

604 Having investigated the multipath performance of the Galileo signals, we then turned our
605 attention into the assessment of the measurement noise. To do so, we made use of the LS-

606 VCE method to estimate the zenith-referenced variance of the signals on different
607 frequencies. Our estimations are combinations of the transmitted signal quality, the receiver
608 architecture including correlator and loops, and any remaining mis-modeled effects like
609 multipath. Describing a multipath mitigation method, we presented the LS-VCE estimations
610 of the mentioned variances for both the original and the multipath-corrected data of several
611 short baselines of different lengths and receiver/antenna types. The order in which the signals
612 can be arranged in terms of their precision is different for various receiver/antenna types.
613 Upon applying the multipath correction, the code standard deviations of all the signals
614 experienced a dramatic reduction. The code standard deviation of the E5 signal showed
615 significantly smaller values with respect to that of the other signals, with low dependency on
616 the receiver/antenna type and the multipath environment. Estimations based on the data of all
617 four short baselines confirmed a standard deviation of about 6 cm without multipath
618 correction and about 1 cm with multipath correction for the E5 code observations. The phase
619 precision estimations either with or without multipath corrections did not show any
620 dependency on the signal type.

621 Showing a significantly lower level of multipath and noise and higher signal power
622 irrespective of the receiver/antenna type, E5 signal was further investigated for its capability
623 in instantaneous RTK positioning. For this purpose, we made use of the observations
624 recorded by all the mentioned baselines. It was shown that the Galileo E5 single-epoch
625 ambiguity resolution IB success rate of about 90% is achievable for all the station pairs upon
626 applying the multipath correction to the E5 data. This means that the Galileo E5 data, if
627 corrected for the multipath effect, can make (almost) instantaneous ambiguity resolution
628 feasible already based on the current constellation. The resultant ambiguity-fixed positioning
629 precision varied as a function of the receiver/antenna type and the extent to which the
630 multipath impact can be mitigated.

631 We showed that the multipath corrections, generated as described in this paper, capture
632 largely the low-frequency multipath components and partly the high-frequency multipath
633 components which are of higher amplitudes and mainly present in the satellite signals
634 received at low elevations. Our results revealed that the residuals of these high-frequency
635 multipath components after applying the multipath corrections can still lead to incorrect
636 fixing of the DD ambiguities.

637

638 **Acknowledgements**

639 The second author is the recipient of an Australian Research Council (ARC) Federation
640 Fellowship (project number FF0883188). The Netherlands data was provided by Mr.
641 Lennard Huisman from Kadaster, the Netherlands. This support is greatly acknowledged. We
642 are also thankful to Dr. Nandakumaran Nadarajah and Dr. Mohammad Choudhury from
643 Curtin University GNSS Research Center, Perth, Australia for providing the data of UWA0
644 station.

645

646 **References**

647 Afifi A, El-Rabbany A (2014) Single Frequency GPS/Galileo Precise Point Positioning
648 Using Un-Differenced and Between-Satellite Single Difference Measurements.
649 GEOMATICA 68:195–205

650

651 Amiri-Simkooei AR, Teunissen PJG, Tiberius CCJM (2009) Application of least-squares
652 variance component estimation to GPS observables. J Surv Eng 135(4):149–160

653 Bock, Y (1991) Continuous monitoring of crustal deformation. GPS World, 2(6), 40 – 47

654

655 de Bakker PF, van der Marel H, Tiberius CC (2009) Geometry-free undifferenced, single and
656 double differenced analysis of single frequency GPS, EGNOS and GIOVE-A/B
657 measurements. GPS solut 13(4):305–314

658

659 de Bakker PF, Tiberius CC, Van Der Marel H, van Bree RJ (2012) Short and zero baseline
660 analysis of GPS L1 C/A, L5Q, GIOVE E1B, and E5aQ signals. GPS solut 16(1):53–64

661

662 Cai C, Luo X, Liu Z, Xiao Q (2014) Galileo Signal and Positioning Performance Analysis
663 Based on Four IOV Satellites. Navigation 67:810–824

664

665 Cai C, Gao Y, Pan L, Zhu J (2015) Precise point positioning with quad-constellations: GPS,
666 BeiDou, GLONASS and Galileo. Adv Space Res 56:133–143

667

668 Cai C, He C, Santerre R, Pan L, Cui X, Zhu J (2016) A comparative analysis of measurement
669 noise and multipath for four constellations: GPS, BeiDou, GLONASS and Galileo. Survey
670 Review 48:287–295

671

672 Cameron A, Reynolds T (2014) Power Loss Created Trouble Aboard Galileo Satellite.
673 Available from Available from:<http://gpsworld.com/trouble-aboard-galileo-satellite/>,
674 published 8 July 2014

675

676 Diessongo TH, Schüler T, Junker S (2014) Precise position determination using a Galileo E5
677 single-frequency receiver. GPS solut 18(1):73–83

678

679 EL-Hattab AI (2013) Influence of GPS antenna phase center variation on precise positioning.
680 NRIAG Journal of Astronomy and Geophysics 2:272-277

681

682 ESA (2016) Galileo Fact Sheet. Available from:
683 <http://esamultimedia.esa.int/docs/galileo/Galileo-factsheet-2016.pdf>

684

685 Estey LH, Meertens CM (1999) TEQC: the multi-purpose toolkit for GPS/GLONASS data.
686 GPS solut 3(1):42–49

687

688 Euler HJ, Goad CC (1991) On optimal filtering of GPS dual frequency observations without
689 using orbit information. Bulletin Geodesique 65(2):130–143

690

691 European Commission (2015) European GNSS (Galileo) Open Service Signal In Space
692 Interface Control Document (OS SIS ICD)

693

694 Gaglione S, Angrisano A, Castaldo G, Freda P, Gioia C, Innac A, Troisi S, Del Core G
695 (2015) The first Galileo FOC satellites: From useless to essential. In: Geoscience and Remote

696 Sensing Symposium (IGARSS), 2015 IEEE International, IEEE, pp 3667–3670, DOI
697 10.1109/IGARSS.2015.732661814

698

699 Genrich JF, Bock Y (1992) Rapid resolution of crustal motion at short ranges with the Global
700 Positioning System. *J. Geophys. Res.*, 97, 3261 – 3269

701

702 Gioia C, Borio D, Angrisano A, Gaglione S, Fortuny-Guasch J (2015) A Galileo IOV
703 assessment: measurement and position domain. *GPS solut* 19:187–199

704

705 GSA (2017) Galileo Programme. [https://www.gsc-europa.eu/galileo-gsc-](https://www.gsc-europa.eu/galileo-gsc-overview/programme)
706 [overview/programme](https://www.gsc-europa.eu/galileo-gsc-overview/programme)

707

708 Guo F, Li X, Zhang X, Wang J (2017) Assessment of precise orbit and clock products for
709 Galileo, BeiDou, and QZSS from IGS Multi-GNSS Experiment (MGEX). *Survey Review*
710 21:279–290

711

712 Hauschild A, Montenbruck O, Sleewaegen JM, Huisman L, Teunissen PJ (2012)
713 Characterization of compass M-1 signals. *GPS solut* 16(1):117–126

714

715 Hellemans A (2014) A simple plumbing problem sent Galileo satellites into wrong orbits.
716 [http://spectrum.ieee.org/tech-talk/aerospace/satellites/a-simple-plumbing-problem-sent-](http://spectrum.ieee.org/tech-talk/aerospace/satellites/a-simple-plumbing-problem-sent-galileo-satellites-into-wrong-orbits)
717 [galileo-satellites-into-wrong-orbits](http://spectrum.ieee.org/tech-talk/aerospace/satellites/a-simple-plumbing-problem-sent-galileo-satellites-into-wrong-orbits)

718

719 Hofmann-Wellenhof B, Lichtenegger H, Wasle E (2008) GNSS-Global Navigation Satellite
720 Systems, GPS, GLONASS, Galileo and more. Springer-Verlag

721

722 Langley R (2014) ESA Discusses Galileo Satellite Power Loss, Upcoming Launch. Available
723 from Available from:[http://gpsworld.com/esa-discusses-galileo-satellite-power-loss-](http://gpsworld.com/esa-discusses-galileo-satellite-power-loss-upcoming-launch/)
724 [upcoming-launch/](http://gpsworld.com/esa-discusses-galileo-satellite-power-loss-upcoming-launch/), published 20 August 2014

725

726 Langley RB, Banville S, Steigenberger P (2012) First results: precise positioning with
727 Galileo prototype satellites. *GPS World* 23:45–49

728

729 Li X, Ge M, Dai X, Ren X, Fritsche M, Wickert J, Schuh H (2015) Accuracy and reliability
730 of multi-GNSS real-time precise positioning: GPS, GLONASS, BeiDou, and Galileo. *J Geod*
731 89:607–635

732

733 Liu T, Yuan Y, Zhang B, Wang N, Tan B, Chen Y (2017) Multi-GNSS precise point
734 positioning (MGPPP) using raw observations. *J Geod* 91(3):253–268

735

736 Lou Y, Zheng F, Gu S, Wang C, Guo H, Feng Y (2016) Multi-GNSS precise point
737 positioning with raw single-frequency and dual-frequency measurement models. *GPS solut*
738 20:849–862

739

740 Mader G (2002) GPS Antenna Calibration at the National Geodetic Survey. National
741 Geodetic Survey, NOS, NOAA, Silver Spring, MD

742

743 Nadarajah N, Teunissen PJG (2014) Instantaneous GPS/Galileo/QZSS/SBAS Attitude
744 Determination: A Single-Frequency (L1/E1) Robustness Analysis under Constrained
745 Environments. *Navigation* 61(1):65–75

746

747 Nadarajah N, Teunissen PJG, Raziq N (2013) Instantaneous GPS–Galileo attitude
748 determination: single-frequency performance in satellite-deprived environments. *IEEE*
749 *Transactions on Vehicular Technology* 62(7):2963–2976

750

751 Nadarajah N, Khodabandeh A, Teunissen PJG (2015) Assessing the IRNSS L5-signal in
752 combination with GPS, Galileo, and QZSS L5/E5a-signals for positioning and navigation.
753 *GPS solut* 20(2):289–297

754

755 Odijk D, Teunissen PJG, Huisman L (2012) First results of mixed GPS+GIOVE single-
756 frequency RTK in Australia. *J Spat Sci* 57(1):3–18

757

758 Odijk D, Teunissen PJG, Khodabandeh A (2014) Galileo IOV RTK positioning: standalone
759 and combined with GPS. *Survey Review* 46:267–277

760

761 Odolinski R, Odijk D, Teunissen PJG (2015) Combined BDS, Galileo, QZSS and GPS
762 single-frequency RTK. *GPS solut* 19:151–163

763

764 Pan L, Cai C, Santerre R, Zhang X (2017) Performance evaluation of single-frequency point
765 positioning with GPS, GLONASS, BeiDou and Galileo. *Survey Review* pp 1–9, DOI
766 10.1080/00396265.2016.1151628

767

768 Simsky A, Sleewaegen JM, Hollreiser M, Crisci M (2006) Performance Assessment of
769 Galileo Ranging Signals Transmitted by GSTB-V2 Satellites. *Proc. ION GNSS 2006*,
770 Institute of Navigation, Fort Worth, Texas, USA, September 26-29, 1547-1559

771

772 Simsky A, Mertens D, Sleewaegen JM, Hollreiser M, Crisci M (2008a) Experimental Results
773 for the Multipath Performance of Galileo Signals Transmitted by GIOVE-A Satellite.
774 *International Journal of Navigation and Observation* pp 1–13, DOI 10.1155/2008/416380

775

776 Simsky A, Sleewaegen JM, Wilde WD, Hollreiser M, Crisci M (2008b) Multipath and
777 Tracking Performance of Galileo Ranging Signals Transmitted by GIOVE-B. *Proc. ION*
778 *GNSS 2008*, Institute of Navigation, Savannah, Georgia, USA, September 16-19, 1525-1536

779

780 Steigenberger P, Montenbruck O (2016) Galileo status: orbits, clocks, and positioning. *GPS*
781 *solut* 21(2):319–331

782

783 Steigenberger P, Hugentobler U, Montenbruck O (2013) First demonstration of Galileo-only
784 positioning. *GPS World* 24:14–15
785

786 Tegedor J, Øvstedal O, Vigen E (2014) Precise orbit determination and point positioning
787 using GPS, Glonass, Galileo and BeiDou. *Journal of Geodetic Science* 4:65–73
788

789 TegedorJ, Øvstedal O, Vigen E (2015) Estimation of Galileo Uncalibrated Hardware Delays
790 for Ambiguity-Fixed Precise Point Positioning. *Navigation* 63:173–179
791

792 Teunissen PJG (1998) Success probability of integer GPS ambiguity rounding and
793 bootstrapping. *J Geod* 72(10):606–612
794

795 Teunissen PJG (1999) An optimality property of the integer least-squares estimator. *J Geod*
796 73(11):587–593
797

798 Teunissen PJG, Amiri-Simkooei AR (2008) Least-squares variance component estimation. *J*
799 *Geod* 82(2):65–82
800

801 Teunissen PJG, Montenbruck O Eds. (2017) *Springer Handbook of Global Navigation*
802 *Satellite Systems*. Springer
803

804 Tranquilla JM, Cam JP, Al-Rizzo HM (1994) Analysis of a Choke Ring Groundplane for
805 Multipath Control in Global Positioning System (GPS) Applications. *IEEE Trans Antennas*
806 *Propag* 42(7):905–911
807

808 Verhagen S, Teunissen PJG (2014) Ambiguity resolution performance with GPS and BeiDou
809 for LEO formation flying. *Adv Space Res* 54(5):830–839
810

811 Zaminpardaz S, Teunissen PJG, Nadarajah N (2016) GLONASS CDMA L3 ambiguity
812 resolution and positioning. GPS solut 21(2):535–549

813

814 **Author Biographies**

815 **Safoora Zaminpardaz** received her MSc in Geodesy from University of Tehran. She has
816 been pursuing her PhD since July 2014 at the GNSS Research Centre, Curtin University,
817 Australia. Her research interests include array-based multi-GNSS positioning, ionosphere
818 sensing and integrity monitoring.

819

820 **Peter J.G. Teunissen** is Professor of Geodesy and Navigation and Head of CUT's GNSS
821 Research Centre. His current research focuses on multi-GNSS and the modelling of next
822 generation GNSS for high-precision positioning, navigation and timing applications.

823